ACS APPLIED MATERIALS & INTERFACES

www.acsami.org

Research Article

Boosted Solar Light Absorbance in PdS_2/PtS_2 Vertical Heterostructures for Ultrathin Photovoltaic Devices

Lorenzo Bastonero, Giancarlo Cicero, Maurizia Palummo, and Michele Re Fiorentin*

Cite This: *ACS Appl. Mater. Interfaces* 2021, 13, 43615–43621

Read Online

ACCESS | Metrics & More | Article Recommendations | Supporting Information

ABSTRACT: Transition-metal dichalcogenides (TMDs) represent a class of materials whose archetypes, such as MoS_2 and WS_2, possess exceptional electronic and optical properties and have been massively exploited in optoelectronic applications. The layered structure allows for their exfoliation to two-dimensional samples with atomic thickness ($\lesssim$ 1 nm), promising for ultrathin, ultralight devices. In this work, by means of state-of-the-art *ab initio* many-body perturbation theory techniques, we focus on single-layer PdS_2 and PtS_2 and propose a novel van der Waals heterostructure with outstanding light absorbance, reaching up to 50% in the visible spectrum and yielding a maximum short-circuit current of 7.2 mA/cm^2 under solar irradiation. The computed excitonic landscape predicts a partial charge separation between the two layers and the momentum-forbidden lowest-energy state increases the carrier diffusion length. Our results show that the employment of vertical heterostructures with less conventional TMDs, such as PdS_2/PtS_2, can greatly boost light absorbance and favor the development of more efficient, atomic-thin photovoltaic devices.

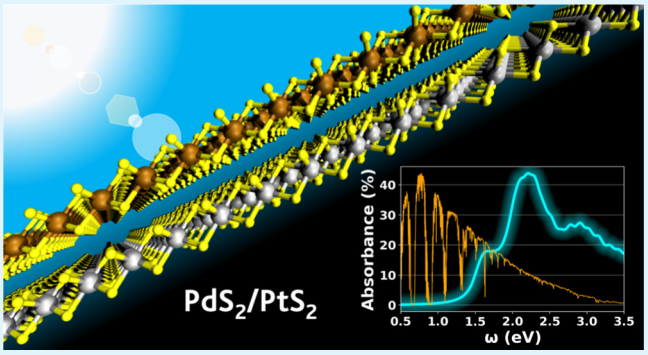

KEYWORDS: *photovoltaics, TMDs, van der Waals heterostructures, 2D materials, excitons*

1. INTRODUCTION

Two-dimensional (2D) materials have elicited great attention over the last few decades thanks to their unique electronic and optical properties induced by their atomic-scale thickness.[1−3] A plethora of materials are currently under investigation, and particular interest has been focused on transition-metal dichalcogenides (TMDs) in their monolayer form. TMDs can be easily exfoliated to single layers and allow for largely tunable optoelectronic properties,[4,5] thanks to the plentiful possible combinations of transition metal and chalcogen species. For instance, band gaps of monolayer TMDs range from 0.5 to 7.0 eV[6] and can be both direct and indirect. This wide range of electronic properties can be further enriched by devising vertical van der Waals heterostructures (vdWHs)[7,8] between a monolayer TMD and another 2D material, such as graphene,[9,10] black or blue phosphorene,[11,12] hexagonal boron nitride,[13,14] or a different TMD monolayer.[15,16] vdWHs make it possible to realize devices that allow for the separation of the optically excited electrons and holes thanks to the valence and conduction band discontinuities of the two composing layers. Together with nanometer thickness and suitable band gaps, this feature makes TMD vdWHs appealing for the design of ultrathin, ultralight photovoltaic devices.[17] In this respect, it is therefore necessary that the composing layers show significant light absorbance within the solar spectrum. For photon energies varying between 1.5 and 3 eV, widely studied TMDs show absorbance values that roughly range from 5 to 25% for MoS_2[18] to 20% for $MoSe_2$ or 17% for WSe_2 and WS_2.[19] Their vdWHs exhibit similar behaviors, for instance, reaching peak values of 10% in MoS_2/WS_2[20] and in $MoSe_2/WSe_2$ or 15% in MoS_2/WSe_2.[21] In combination with the incident AM1.5G solar flux $\Phi_s(\omega)$,[22] the absorbance $\mathrm{Abs}(\omega)$ determines the maximum short-circuit current that can be extracted from the solar cell as

$$J_{sc}^{max} = e\int d\omega \mathrm{Abs}(\omega)\Phi_s(\omega) \quad (1)$$

assuming that all photogenerated charge carriers are collected. Common amorphous Si−H and GaAs solar cells in a single-pass configuration show J_{sc}^{max} values which lie around 25 and 35 mA/cm^2, for sample thicknesses above 1 μm, and quickly drop much below 1 mA/cm^2 when their thickness is decreased to around 1 nm.[23] In contrast, it has been predicted that a 1 nm-thick MoS_2/WS_2 vdWH displays a $J_{sc}^{max} \simeq 3.5$ mA/cm^2,[20] the same value obtained in Si−H or GaAs cells about 1 order of

Received: June 16, 2021
Accepted: July 29, 2021
Published: September 1, 2021

https://doi.org/10.1021/acsami.1c11245
ACS Appl. Mater. Interfaces 2021, 13, 43615−43621

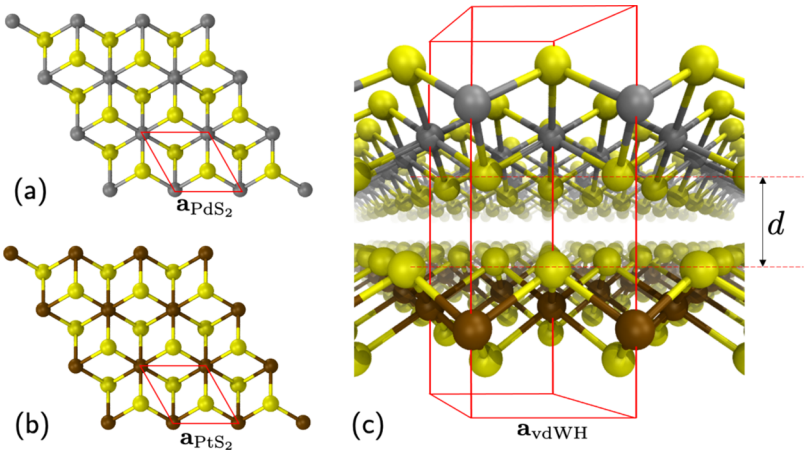

Figure 1. Monolayer PdS_2 (a) and PtS_2 (b) in the 1T phase. (c) Perspective view of the PdS_2/PtS_2 heterostructure with marked unit cell and lattice parameter a_{vdW} and layer separation d.

magnitude thicker. The nanoscale thickness of the heterostructure allows for the design of ultralight devices with high power densities,[24] even though the J_{sc}^{max} remains low on an absolute scale. Higher short-circuit currents can be obtained by suitable arrangements of multiple heterostructures, albeit at the expense of the overall device thinness. Increasing the absorbance of the heterostructure, while keeping its thickness within ∼1 nm, is then of key importance for the development of new nanoscale photovoltaic devices that can introduce a paradigm shift in solar energy harvesting.

In this work, we focus on two less-studied single-layer TMDs which hold great potential, both as distinct monolayers and as part of a vdWH: PdS_2 and PtS_2. Single-layer PtS_2 has been experimentally obtained from bulk PtS_2[25,26] *via* exfoliation[27,28] and reported to be in the 1T phase, Figure 1b. Monolayer PdS_2 has been investigated in its 1T phase,[29] Figure 1a, and its exfoliation process from bulk crystals has been suggested.[30] The lattice parameters and electronic properties of 1T-PtS_2 and 1T-PdS_2, as reported in the literature,[6] suggest the possibility of realizing a low-strain vdWH with type-II band alignment. We therefore propose and investigate a novel 1T-PdS_2/1T-PtS_2 vdWH by employing state-of-the-art *ab initio* simulations, based on density functional theory (DFT) for geometry optimization and the GW-Bethe Salpeter[31,32] approach for the study of optoelectronic properties.

2. METHODS

2.1. DFT Calculations. All the DFT calculations reported in this work were performed using the Quantum ESPRESSO suite.[33−35] For all systems, we employed the Perdew−Burke−Ernzerhof functional[36] and fully relativistic, norm-conserving pseudopotentials[37] on a uniform 4 × 4 × 1 Monkhorst−Pack k-point mesh.[38] A kinetic energy cutoff of 70 Ry was adopted. We introduced a 20 Å vacuum region along z, the direction perpendicular to the layer planes, to ensure the decoupling of the periodic replicas. In the studied systems, spin−orbit coupling effects can be sizeable and were accounted for in all calculations by means of a fully spinorial treatment.[39,40] Dispersion forces between the layers of the heterostructure were reproduced within the DFT-D3 semiempirical model.[41] Structure relaxation was assumed at convergence when the maximum component of the residual forces on the ions was smaller than 10^{-4} Ry/Bohr.

2.2. Many-Body Perturbation Theory Calculations. The optimized structures were studied by means of many-body perturbation theory methods as implemented in the YAMBO code.[42,43] The quasiparticle (QP) electronic structure was obtained within the non-self-consistent G_0W_0 approximation. A box cutoff along z was applied on the bare Coulomb potential. The inverse dielectric matrix, $\varepsilon^{-1}_{GG'}$, was obtained within the Godby-Needs plasmon-pole approximation model.[44,45] As a convergence parameter, we adopted the QP band gap value at the Γ point and deemed satisfactory a convergence of this value within 50 meV. Convergence of the G_0W_0 calculations with respect to the simulation parameters is shown in Figure S1 in Supporting Information. Following the chosen convergence criterion, we chose a 20 × 20 × 1 k-point mesh for all structures.

For both PdS_2 and PtS_2, 2000 bands were included in the calculation of the dielectric function $\varepsilon^{-1}_{GG'}$ and a 20 Ry cutoff was set on the G vectors in ε^{-1}.

Following ref6, we obtain the correction to the band gap due to the number of bands included in the correlation self-energy Σ_c by extrapolation to the limit of infinite bands, cf. Supporting Information, Figure S1c. For PdS_2 and PtS_2 monolayers, the calculations can then be performed with 1000 bands explicitly included in the sum and then corrected by the application of a rigid scissor operator of −0.12 eV. For the vdWH, we employ 4000 bands and 20 Ry in the calculation of the dielectric matrix and 1000 bands in Σ_c, thanks to the adoption of Bruneval−Gonze terminators.[46]

Convergence of the BSE calculations with respect to the simulation parameters is shown in Figure S2 in Supporting Information. For PdS_2 and PtS_2, convergence is reached on a 30 × 30 × 1 grid, with 200 bands and a 2 Ry cutoff on the static screening and 6 valence +6 conduction bands in the BSE kernel. In the case of the vdWH, the number of included bands is doubled.

3. RESULTS AND DISCUSSION

From our DFT calculations, we compute the equilibrium lattice parameters of the isolated monolayers to be a_{PdS2} = 3.53 Å for 1T-PdS_2 and a_{PtS2} = 3.56 Å for 1T-PtS_2, in excellent agreement with the literature.[47] By vertically stacking the two monolayers in the AA configuration,[48] we obtain the vdWH geometry represented in Figure 1c, whose equilibrium lattice parameter results in a_{vdWH} = 3.57 Å and interlayer distance in d = 2.4 Å. The increase in the lattice parameter in the heterostructure can be traced back to the interaction between the layers and the reduced screening, as happens for multilayers of both PdS_2 and PtS_2.[49,50] The resulting strain can be estimated as $\varepsilon_i = (a_{vdWH} - a_i)/a_i$ with i = PtS_2 and PdS_2. The highest value of ε is obtained for the PdS_2 layer, which is subject to about 1.1% tensile strain with respect to its equilibrium geometry. Hence, the monolayers undergo a very mild strain, which does not significantly affect the electronic properties of the system (c.f. Figure S3a in Supporting

https://doi.org/10.1021/acsami.1c11245
ACS Appl. Mater. Interfaces 2021, 13, 43615−43621

Information). The equilibrium geometries of the isolated monolayers and the vdWH are used to compute the electronic band structure at the G_0W_0 level, as reported in Figure 2. On

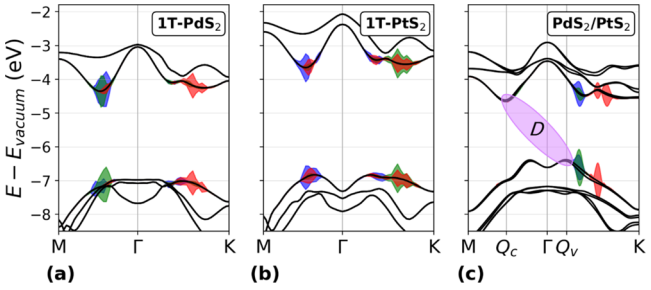

Figure 2. G_0W_0 band structures of (a) 1T-PdS_2, (b) 1T-PtS_2, and (c) PdS_2/PtS_2 vdWH aligned to the vacuum level. The shaded areas in red, green, and blue mark the excitonic weights of the R, G, and B states, respectively (see Figure 3). The violet ellipse in (c) indicates the indirect exciton D with finite momentum $\mathbf{q}_D$.

top of the G_0W_0 quasiparticle energies, we solve the Bethe–Salpeter equation to obtain the light absorption spectrum and excitonic properties, Figure 3. 1T-PdS_2, Figure 2a, presents a

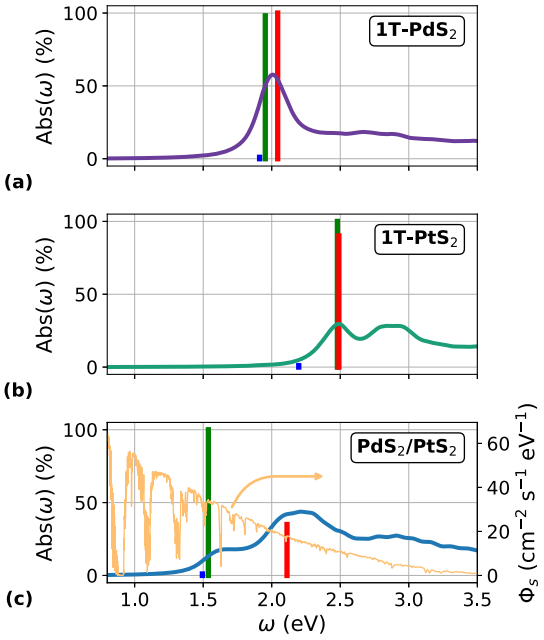

Figure 3. Absorbance Abs(ω) of (a) 1T-PdS_2, (b) 1T-PtS_2, and (c) PdS_2/PtS_2 vdWH. The vertical bars mark the position and relative intensities of the R, G, and B excitons, respectively. In (c), the AM1.5G solar spectrum $\Phi_s(\omega)$ is reported in light yellow.

top valence band (tVB) with a flattened parabolic structure around the Γ point and a conduction band minimum (CBm) at a k-point intermediate between M and Γ, resulting in an indirect band gap $E^{g}_{PdS_2} = 2.50$ eV and a direct gap $E^{g,dir}_{PdS_2} = 2.70$ eV in correspondence with the CBm. The optical absorbance Abs(ω) is shown in Figure 3a, together with the lowest-energy exciton (blue) and the two brightest states (red and green) contributing to the absorption peak. Their energies and binding energies are reported in Table 1. The shaded areas in Figure 2a mark the excitonic weights of excitons B (blue), G (green), and R (red), projected on the QP band structure. From the shaded regions in Figure 2a, it is possible to notice that the strongest transitions contributing to the excitons, rather than occurring at high symmetry points, take place at k-points at which the valence and conduction bands present a similar slope along the k-path, giving rise to the band-nesting phenomenon.[51] This feature is responsible for large divergencies in the joint density of states (jDOS) which, in turn, influences the material dielectric function, enhancing light absorption. We notice that the absorption peak of monolayer 1T-PdS_2 falls around 2 eV and, remarkably, its absorbance reaches up to 55% in that range.

1T-PtS_2, Figure 2b, shows a peculiar Mexican-hat-shaped tVB, with a valence band maximum (VBM) and CBm midway between M and Γ. Although VBM and CBm are closer in k-space, the resulting band gap is nonetheless indirect, $E^{g}_{PtS_2} = 3.05$ eV, while the direct gap is $E^{g,dir}_{PtS_2} = 3.1$ eV. The absorbance spectrum, Figure 3b, is blue-shifted with respect to 1T-PdS_2: the absorption peak is due to two excitons (green and red), at around 2.5 eV, and a dark exciton (blue) is the lowest-energy state, about 30 meV below. The peak in absorbance of PtS_2 is lower than the one of PdS_2 and reaches about 30%. Such a difference in absorbance can be traced back to the different orbital character of the electronic states in the tVB and bCB of the two monolayers. In PdS_2, we observe a sizeable participation of sulfur p orbitals in the tVB states, in contrast to PtS_2, where S p and Pt d orbitals are almost equally contributing to the topmost valence band (c.f. Supporting Information Figures S4 and S5). The difference in the orbital character results in a stronger band-nesting for PdS_2 which, consequently, increases the jDOS, as shown in Figure S6a,b. Moreover, we determined that the independent-particle electric dipole matrix elements $d_{cv}\mathbf{k}$ of the transitions $v \rightarrow c$ at $\mathbf{k}$, contributing to the absorption peak, are larger in PdS_2 than in PtS_2, c.f. Figure S6c. The larger jDOS and the stronger dipole elements thus cooperate to enhance the optical absorption of PdS_2 with respect to PtS_2.

In Figure 3b, at around 2.8 eV, it is also possible to notice a broader peak in the absorbance spectrum, originating from states, close in energy, whose main dipole transitions involve the bCB and tVB-1.

Although less pronounced than in PdS_2, the contribution from the p-orbitals of the outer S layers to the tVB of PtS_2 is non-negligible, Figure S4. Therefore, in a vdWH, the tVB of each monolayer is significantly affected by the presence of the facing one, resulting in a vdWH tVB which shows sizeable

Table 1. Transition Energies E_λ [eV] and Exciton Binding Energies E_b [eV] of the Analyzed Excitons (B = Blue; R = Red; and G = Green)

	1T-PdS2			1T-PtS2			1T-PdS2/1T-PtS2		
	B	G	R	B	G	R	B	G	R
E_λ	1.91	1.95	2.04	2.20	2.48	2.49	1.49	1.53	2.11
E_b	0.8	0.8	0.7	0.9	0.6	0.6	0.7	0.6	0.1

https://doi.org/10.1021/acsami.1c11245
ACS Appl. Mater. Interfaces 2021, 13, 43615−43621

contributions from both PdS_2 and PtS_2 valence band states. In Figure 4, we show the *k*-resolved density of states (DOS) of

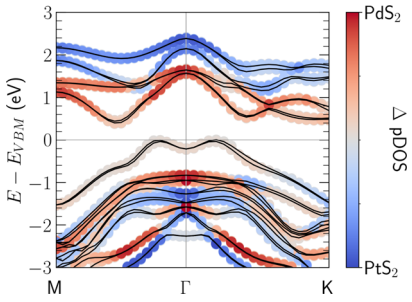

Figure 4. 1T-PdS_2/1T-PtS_2 vdWH *k*-resolved projected density of states superimposed to the DFT band structure. Each state is colored according to the size of the contributions from PdS_2 (red) and PtS_2 (blue) orbitals.

the 1T-PdS_2/1T-PtS_2 heterostructure, projected on the orbitals of the atoms composing the two layers. The bands along the *k*-path are colored according to the difference between the DOS contributions from the two layers, allowing us to identify on which layer the electronic states at various *k*-points are spatially localized. As mentioned, the vdWH tVB shows some degree of delocalization on both layers, while the bCB, being mostly composed of inner metal d-orbitals, is less affected by the interlayer interactions and clearly localized on 1T-PdS_2. The G_0W_0-corrected band structure, aligned to the vacuum level, is reported in Figure 2c. In contrast to the isolated monolayers, in the vdWH case, the inversion symmetry is broken; hence, its band structure shows spin−orbit splitting. The band gap is indirect, E^{g}_{vdWH} = 1.72 eV, between *k*-points $\mathbf{Q}_c$ and $\mathbf{Q}_v$, and notably smaller than each monolayer's. The direct band gap is found to be $E^{g,dir}_{vdWH}$ = 2.17 eV in correspondence with $\mathbf{Q}_v$. The electronic band gap reduction is an expected feature linked to the type-II alignment of the single TMD band structures, cf. Figure 2a,b, and the interaction between the two layers, which determines an upshift of the top valence band, and the increased electronic screening. This similarly entails a reduction in the optical band gap, as shown in Figure 3c. The absorption onset red-shifts to about 1.5 eV and stems from a bright exciton (labeled "green", G) at 1.53 eV, c.f. Table 1. This exciton is almost degenerate in energy with the lowest-energy, dark state (blue, B), whose constituting transitions take place at the same *k*-points as the green exciton but connect states with the opposite spin.

By means of eq 1 and the absorbance spectra in Figure 3, we can compute the maximum short-circuit currents that can be extracted from the monolayers and from the vdWH, in the idealized situation of total carrier collection at the electrodes. 1T-PtS_2 has a higher-energy absorption edge and a moderate absorption, resulting in J^{max}_{sc} = 1.9 mA/cm^2, while 1T-PdS_2 shows a lower absorption onset and outstanding absorbance values so that its maximum short-circuit current reaches 5.4 mA/cm^2. The vdWH shows less pronounced absorbance peaks than 1T-PdS_2; however, the optical gap falls at lower energy, optimizing sunlight absorption in the visible range. Hence, the short-circuit current of the heterostructure reaches 7.2 mA/cm^2, slightly lower than the sum of the J^{max}_{sc} of the isolated monolayers. The predicted value of maximum short-circuit current is exceptionally high and can largely boost the efficiency of a device made with such a vdWH. As a comparison, the obtained maximum short-circuit current is twice the predicted value in MoS_2/WS_2 vdWH[20] and can be obtained with amorphous Si−H samples about 2 orders of magnitude thicker.

The brightest excitons, red and green, which induce the peaks in the absorption spectrum of the vdWH, vertically excite electrons and holes at *k*-points away from the CBm and VBM, respectively. In mono- and few-layer TMDs, intraband relaxation is very fast ($\lesssim$500 fs);[52,53] therefore, we can expect a rapid relaxation of the optically active excitons to the dark, indirect exciton *D*, involving states at the CBm and VBM, violet ellipse in Figure 2c. The relaxation to this exciton, with finite momentum $\boldsymbol{q}_D = \mathbf{Q}_c - \mathbf{Q}_v$, is energetically favorable, since E_D = 1.15 eV, smaller than the dark direct exciton *B*. Being momentum-forbidden, the radiative recombination of state *D* is suppressed and, consequently, its lifetime is largely enhanced with respect to bright excitons.[54] Electron−hole recombination is therefore slowed down, and the carrier diffusion length increased. Hence, due to the indirect gap in the 1T-PdS_2/1T-PdS_2 heterostructure, we expect carrier diffusion lengths longer than 20 μm, as recently measured in the direct-gap WS_2/WSe_2 vdWH.[55] The expected sizeable diffusion length will then contribute to enhance the actual short-circuit current of the real device, by increasing the

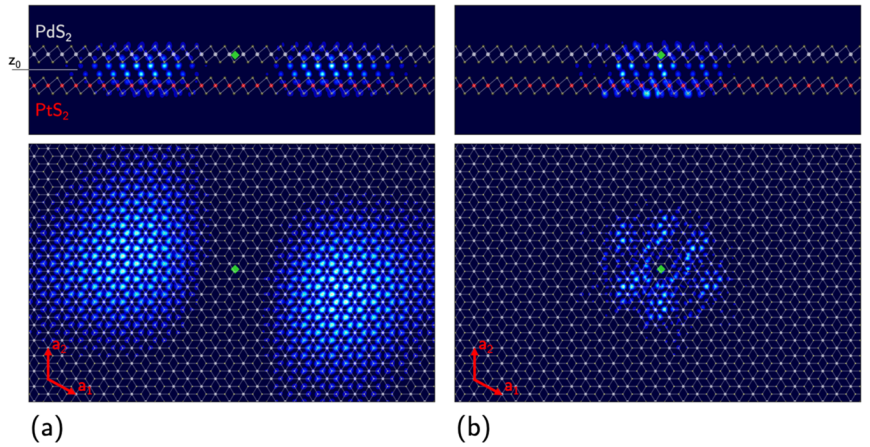

Figure 5. Side (upper panels) and top (lower panels) views of the square modulus excitonic wave function $|\Psi_\lambda(\boldsymbol{r}_h|\mathbf{r}_e = \boldsymbol{r}')|^2$ for states $\lambda = D$ (a) and $\lambda = G$ (b). In both (a,b), the electron is marked by the green diamond and kept fixed on PdS_2.

https://doi.org/10.1021/acsami.1c11245
ACS Appl. Mater. Interfaces 2021, 13, 43615−43621

collection probability, thus positively impacting on the efficiency of the cell. These efficiency boosting factors, that is, very large absorbance and increased diffusion length, can then counterbalance the limited charge separation due to the mixed PdS_2−PtS_2 states in the tVB, c.f. Figure 4, that could also act as recombination centers. Indeed, the optically excited electrons will populate states which are well spatially localized on the PdS_2 layer, while the holes will still present a sizeable delocalization on both monolayers. In Figure 5a, we show the square modulus of the *D* exciton wave function as a function of the hole position $|\Psi_D(\mathbf{r}_h|\mathbf{r}_e = r')|^2$, when the electron is fixed at r' on the PdS_2 layer, in a region with maximum probability density. The electron is marked by the green diamond on the PdS_2 layer. The electron and hole show a peculiar in-plane spatial separation, due to the electronic orbitals involved in *D*. As a comparison, in Figure 5b, we report the square modulus of the bright, *G* exciton wave function, with fixed electron in the same position. It is evident that the *G* and *D* excitons are not spatially indirect between the two layers, and their wave functions involve both PdS_2 and PtS_2. From Figure 5a, it is possible to notice that the hole is fairly delocalized on both layers and it is possible to obtain the probability of finding the hole on the PtS_2 layer as $\int_{z_h<z_0} dr_h |\Psi_D(r_h|r_e = r')|^2 \simeq 50\%$, where z_0 defines the intermediate plane between the two monolayers. This provides us with an estimate of the charge separation probability, given that the hole distribution varies little when the electron position is moved in the region of sizeable probability density, concentrated on PdS_2. The estimated charge separation is not complete, however, its magnitude, combined with the encouraging properties previously highlighted, can be nonetheless adequate for viable applications of the proposed vdWH. Moreover, it has been proven that spatially indirect excitons inducing interlayer charge separation can be enhanced by applying strain[56,57] to the heterostructure or controlled through electric fields,[58] thus conceivably leaving room for further efficiency improvements.

4. CONCLUSIONS

The field of nanoscale photovoltaic devices is still in open development and appears alluring for its potential to compete with conventional systems. The intrinsic advantages of ultrathin, ultralight devices urge the research activities toward improved efficiency and design. The employment of monolayer TMDs in heterostructures has been proposed and investigated, with most attention paid to group-VI TMDs, such as MoS_2 and WS_2, which have provided encouraging results. A key factor for choosing TMDs for this type of application resides in their large light-electron coupling, which results in sizeable light absorbance. Our work unveiled the remarkable properties of two, less common, TMDs, PdS_2 and PtS_2, which can be positively employed in the domain of photovoltaics. In particular, the uncommon absorbance of 1T-PdS_2 is inherited by the low-strain vdWH with PtS_2, which also shows a very favorable optical gap at around 1.5 eV. This translates into exceptionally high maximum short-circuit currents, $J_{sc}^{max} = 7.2$ mA/cm^2, about twice the values previously reported for MoS_2/WS_2 vdWH. Although the predicted charge separation is partial, the high absorbance, together with the extended carrier diffusion length, due to the indirect electronic band gap, can turn out very advantageous for improving the efficiency of nanometer-thick photovoltaic devices.

ASSOCIATED CONTENT

Supporting Information

The Supporting Information is available free of charge at https://pubs.acs.org/doi/10.1021/acsami.1c11245.

G_0W_0 and BSE convergence tests, details on PdS_2 and PtS_2 monolayer optical absorbance, and selected wave functions (PDF)

AUTHOR INFORMATION

Corresponding Author

Michele Re Fiorentin − *Center for Sustainable Future Technologies, Istituto Italiano di Tecnologia, 10144 Torino, Italy;* orcid.org/0000-0002-1074-0411; Email: michele.refiorentin@iit.it

Authors

Lorenzo Bastonero − *U Bremen Excellence Chair "Materials Design and Discovery" and Hybrid Materials Interfaces Group, Bremen Center for Computational Materials Science, University of Bremen, 28359 Bremen, Germany; Dipartimento di Fisica, Università Degli Studi Torino, 10125 Torino, Italy;* orcid.org/0000-0001-9374-1876

Giancarlo Cicero − *Dipartimento di Scienza Applicata e Tecnologia, Politecnico di Torino, 10129 Torino, Italy;* orcid.org/0000-0002-2920-9882

Maurizia Palummo − *Dipartimento di Fisica and INFN, Università di Roma "Tor Vergata", 00133 Roma, Italy;* orcid.org/0000-0002-3097-8523

Complete contact information is available at: https://pubs.acs.org/10.1021/acsami.1c11245

Notes

The authors declare no competing financial interest.

ACKNOWLEDGMENTS

We acknowledge CINECA for the availability of high-performance computing resources under the Iscra-B initiative, and the computational facilities and support provided by HPC@POLITO.

REFERENCES

(1) Bhimanapati, G. R.; Lin, Z.; Meunier, V.; Jung, Y.; Cha, J.; Das, S.; Xiao, D.; Son, Y.; Strano, M. S.; Cooper, V. R.; Liang, L.; Louie, S. G.; Ringe, E.; Zhou, W.; Kim, S. S.; Naik, R. R.; Sumpter, B. G.; Terrones, H.; Xia, F.; Wang, Y.; Zhu, J.; Akinwande, D.; Alem, N.; Schuller, J. A.; Schaak, R. E.; Terrones, M.; Robinson, J. A. Recent Advances in Two-Dimensional Materials Beyond Graphene. *ACS Nano* **2015**, *9*, 11509−11539.

(2) Tan, T.; Jiang, X.; Wang, C.; Yao, B.; Zhang, H. 2D Material Optoelectronics for Information Functional Device Applications: Status and Challenges. *Adv. Sci.* **2020**, *7*, 2000058.

(3) Kang, S.; Lee, D.; Kim, J.; Capasso, A.; Kang, H. S.; Park, J.-W.; Lee, C.-H.; Lee, G.-H. 2D Semiconducting Materials for Electronic and Optoelectronic Applications: Potential and Challenge. *2D Materials* **2020**, *7*, 022003.

(4) Huang, H. H.; Fan, X.; Singh, D. J.; Zheng, W. T. Recent Progress of TMD Nanomaterials: Phase Transitions and Applications. *Nanoscale* **2020**, *12*, 1247−1268.

(5) Manzeli, S.; Ovchinnikov, D.; Pasquier, D.; Yazyev, O. V.; Kis, A. 2D Transition Metal Dichalcogenides. *Nat. Rev. Mater.* **2017**, *2*, 17033.

(6) Rasmussen, F. A.; Thygesen, K. S. Computational 2D Materials Database: Electronic Structure of Transition-Metal Dichalcogenides and Oxides. *J. Phys. Chem. C* **2015**, *119*, 13169−13183.

(7) Liu, Y.; Weiss, N. O.; Duan, X.; Cheng, H.-C.; Huang, Y.; Duan, X. Van Der Waals Heterostructures and Devices. *Nat. Rev. Mater.* **2016**, *1*, 16042.
(8) Geim, A. K.; Grigorieva, I. V. Van Der Waals Heterostructures. *Nature* **2013**, *499*, 419−425.
(9) Li, C.; Cao, Q.; Wang, F.; Xiao, Y.; Li, Y.; Delaunay, J.-J.; Zhu, H. Engineering Graphene and TMDs Based Van Der Waals Heterostructures for Photovoltaic and Photoelectrochemical Solar Energy Conversion. *Chem. Soc. Rev.* **2018**, *47*, 4981−5037.
(10) Azadmanjiri, J.; Srivastava, V. K.; Kumar, P.; Sofer, Z.; Min, J.; Gong, J. Graphene-Supported 2D Transition Metal Dichalcogenide Van Der Waals Heterostructures. *Appl. Mater. Today* **2020**, *19*, 100600.
(11) Peng, Q.; Wang, Z.; Sa, B.; Wu, B.; Sun, Z. Electronic Structures and Enhanced Optical Properties of Blue Phosphorene/Transition Metal Dichalcogenides Van Der Waals Heterostructures. *Sci. Rep.* **2016**, *6*, 31994.
(12) Maniyar, A.; Choudhary, S. Visible Region Absorption in TMDs/phosphorene Heterostructures for Use in Solar Energy Conversion Applications. *RSC Adv.* **2020**, *10*, 31730−31739.
(13) Latini, S.; Winther, K. T.; Olsen, T.; Thygesen, K. S. Interlayer Excitons and Band Alignment in MoS2/hBN/WSe2 Van Der Waals Heterostructures. *Nano Lett.* **2017**, *17*, 938−945.
(14) Jadczak, J.; Kutrowska-Girzycka, J.; Bieniek, M.; Kazimierczuk, T.; Kossacki, P.; Schindler, J. J.; Debus, J.; Watanabe, K.; Taniguchi, T.; Ho, C. H.; Wójs, A.; Hawrylak, P.; Bryja, L. Probing Negatively Charged and Neutral Excitons in MoS2/hBN and hBN/MoS2/hBN Van Der Waals Heterostructures. *Nanotechnology* **2021**, *32*, 145717.
(15) Huo, N.; Yang, Y.; Li, J. Optoelectronics Based on 2D TMDs and Heterostructures. *J. Semiconduct.* **2017**, *38*, 031002.
(16) Saha, D.; Varghese, A.; Lodha, S. Atomistic Modeling of Van Der Waals Heterostructures With Group-6 and Group-7 Monolayer Transition Metal Dichalcogenides for Near Infrared/Short-Wave Infrared Photodetection. *ACS Appl. Nano Mater.* **2020**, *3*, 820−829.
(17) Furchi, M. M.; Höller, F.; Dobusch, L.; Polyushkin, D. K.; Schuler, S.; Mueller, T. Device Physics of Van Der Waals Heterojunction Solar Cells. *npj 2D Mater. Appl.* **2018**, *2*, 3.
(18) Li, Y.; Chernikov, A.; Zhang, X.; Rigosi, A.; Hill, H. M.; van der Zande, A. M.; Chenet, D. A.; Shih, E.-M.; Hone, J.; Heinz, T. F. Measurement of the optical dielectric function of monolayer transition-metal dichalcogenides:MoS2,MoSe2,WS2, andWSe2. *Phys. Rev. B: Condens. Matter Mater. Phys.* **2014**, *90*, 205422.
(19) Wurstbauer, U.; Miller, B.; Parzinger, E.; Holleitner, A. W. Light-matter interaction in transition metal dichalcogenides and their heterostructures. *J. Phys. D: Appl. Phys.* **2017**, *50*, 173001.
(20) Bernardi, M.; Palummo, M.; Grossman, J. C. Extraordinary Sunlight Absorption and One Nanometer Thick Photovoltaics Using Two-Dimensional Monolayer Materials. *Nano Lett.* **2013**, *13*, 3664−3670.
(21) Flöry, N.; Jain, A.; Bharadwaj, P.; Parzefall, M.; Taniguchi, T.; Watanabe, K.; Novotny, L. A WSe2/MoSe2 Heterostructure Photovoltaic Device. *Appl. Phys. Lett.* **2015**, *107*, 123106.
(22) National Renewable Energy Laboratory. Solar Spectra. http://rredc.nrel.gov/solar/spectra/am1.5/ (accessed 30 March 2021).
(23) Andreani, L. C.; Bozzola, A.; Kowalczewski, P.; Liscidini, M.; Redorici, L. Silicon Solar Cells: Toward the Efficiency Limits. *Adv. Phys.: X* **2019**, *4*, 1548305.
(24) Jariwala, D.; Davoyan, A. R.; Wong, J.; Atwater, H. A. Van Der Waals Materials for Atomically-Thin Photovoltaics: Promise and Outlook. *ACS Photonics* **2017**, *4*, 2962−2970.
(25) Furuseth, S.; Selte, K.; Kjekshus, A.; Gronowitz, S.; Hoffman, R. A.; Westerdahl, A. Redetermined Crystal Structures of NiTe2, PdTe2, PtS2, PtSe2, and PtTe2. *Acta Chem. Scand.* **1965**, *19*, 257−258.
(26) Hulliger, F. Electrical Properties of Some Nickel-Group Chalcogenides. *J. Phys. Chem. Solids* **1965**, *26*, 639−645.
(27) Zhao, Y.; Qiao, J.; Yu, P.; Hu, Z.; Lin, Z.; Lau, S. P.; Liu, Z.; Ji, W.; Chai, Y. Extraordinarily Strong Interlayer Interaction in 2D Layered PtS2. *Adv. Mater.* **2016**, *28*, 2399−2407.
(28) Tang, C. Y.; Cheng, P. K.; Wang, X. Y.; Ma, S.; Long, H.; Tsang, Y. H. Size-Dependent Nonlinear Optical Properties of Atomically Thin PtS2 Nanosheet. *Opt. Mater.* **2020**, *101*, 109694.
(29) Miró, P.; Ghorbani-Asl, M.; Heine, T. Two Dimensional Materials Beyond MoS2: Noble-Transition-Metal Dichalcogenides. *Angew. Chem., Int. Ed.* **2014**, *53*, 3015−3018.
(30) Wang, Y.; Li, Y.; Chen, Z. Not your familiar two dimensional transition metal disulfide: structural and electronic properties of the PdS2monolayer. *J. Mater. Chem. C* **2015**, *3*, 9603.
(31) Onida, G.; Reining, L.; Rubio, A. Electronic excitations: density-functional versus many-body Green's-function approaches. *Rev. Mod. Phys.* **2002**, *74*, 601−659.
(32) Martin, R.; Reining, L.; Ceperley, D. *Interacting Electrons: Theory and Computational Approaches*; Cambridge University Press, 2016.
(33) Giannozzi, P.; Baroni, S.; Bonini, N.; Calandra, M.; Car, R.; Cavazzoni, C.; Ceresoli, D.; Chiarotti, G. L.; Cococcioni, M.; Dabo, I.; Dal Corso, A.; de Gironcoli, S.; Fabris, S.; Fratesi, G.; Gebauer, R.; Gerstmann, U.; Gougoussis, C.; Kokalj, A.; Lazzeri, M.; Martin-Samos, L.; Marzari, N.; Mauri, F.; Mazzarello, R.; Paolini, S.; Pasquarello, A.; Paulatto, L.; Sbraccia, C.; Scandolo, S.; Sclauzero, G.; Seitsonen, A. P.; Smogunov, A.; Umari, P.; Wentzcovitch, R. M. QUANTUM ESPRESSO: A Modular and Open-Source Software Project for Quantum Simulations of Materials. *J. Phys.: Condens. Matter* **2009**, *21*, 395502.
(34) Giannozzi, P.; Andreussi, O.; Brumme, T.; Bunau, O.; Buongiorno Nardelli, M.; Calandra, M.; Car, R.; Cavazzoni, C.; Ceresoli, D.; Cococcioni, M.; Colonna, N.; Carnimeo, I.; Dal Corso, A.; de Gironcoli, S.; Delugas, P.; DiStasio, R. A.; Ferretti, A.; Floris, A.; Fratesi, G.; Fugallo, G.; Gebauer, R.; Gerstmann, U.; Giustino, F.; Gorni, T.; Jia, J.; Kawamura, M.; Ko, H.-Y.; Kokalj, A.; Küçükbenli, E.; Lazzeri, M.; Marsili, M.; Marzari, N.; Mauri, F.; Nguyen, N. L.; Nguyen, H.-V.; Otero-de-la-Roza, A.; Paulatto, L.; Poncé, S.; Rocca, D.; Sabatini, R.; Santra, B.; Schlipf, M.; Seitsonen, A. P.; Smogunov, A.; Timrov, I.; Thonhauser, T.; Umari, P.; Vast, N.; Wu, X.; Baroni, S. Advanced Capabilities for Materials Modelling With Quantum ESPRESSO. *J. Phys.: Condens. Matter* **2017**, *29*, 465901.
(35) Giannozzi, P.; Baseggio, O.; Bonfà, P.; Brunato, D.; Car, R.; Carnimeo, I.; Cavazzoni, C.; de Gironcoli, S.; Delugas, P.; Ferrari Ruffino, F.; Ferretti, A.; Marzari, N.; Timrov, I.; Urru, A.; Baroni, S. QuantumESPRESSO toward the exascale. *J. Chem. Phys.* **2020**, *152*, 154105.
(36) Perdew, J. P.; Burke, K.; Ernzerhof, M. Generalized Gradient Approximation Made Simple. *Phys. Rev. Lett.* **1996**, *77*, 3865−3868.
(37) Hamann, D. Optimized Norm-Conserving Vanderbilt Pseudopotentials. *Phys. Rev. B: Condens. Matter Mater. Phys.* **2013**, *88*, 085117.
(38) Monkhorst, H. J.; Pack, J. D. Special Points for Brillouin-Zone Integrations. *Phys. Rev. B: Condens. Matter Mater. Phys.* **1976**, *13*, 5188−5192.
(39) Corso, A. D.; Conte, A. M. Spin-Orbit Coupling With Ultrasoft Pseudopotentials: Application to Au and Pt. *Phys. Rev. B: Condens. Matter Mater. Phys.* **2005**, *71*, 115106.
(40) Marsili, M.; Molina-Sánchez, A.; Palummo, M.; Sangalli, D.; Marini, A. Spinorial formulation of the GW -BSE equations and spin properties of excitons in two-dimensional transition metal dichalcogenides. *Phys. Rev. B* **2021**, *103*, 155152.
(41) Grimme, S. Semiempirical GGA-type Density Functional Constructed With a Long-Range Dispersion Correction. *J. Comput. Chem.* **2006**, *27*, 1787−1799.
(42) Marini, A.; Hogan, C.; Grüning, M.; Varsano, D. Yambo: An Ab Initio Tool for Excited State Calculations. *Comput. Phys. Commun.* **2009**, *180*, 1392.
(43) Sangalli, D.; Ferretti, A.; Miranda, H.; Attaccalite, C.; Marri, I.; Cannuccia, E.; Melo, P.; Marsili, M.; Paleari, F.; Marrazzo, A.; Prandini, G.; Bonfà, P.; Atambo, M. O.; Affinito, F.; Palummo, M.; Molina-Sánchez, A.; Hogan, C.; Grüning, M.; Varsano, D.; Marini, A. Many-Body Perturbation Theory Calculations Using the Yambo Code. *J. Phys.: Condens. Matter* **2019**, *31*, 325902.

https://doi.org/10.1021/acsami.1c11245
ACS Appl. Mater. Interfaces 2021, 13, 43615−43621

(44) Godby, R. W.; Needs, R. J. Metal-Insulator Transition in Kohn-Sham Theory and Quasiparticle Theory. *Phys. Rev. Lett.* **1989**, *62*, 1169−1172.
(45) Rojas, H. N.; Godby, R. W.; Needs, R. J. Space-Time Method forAb InitioCalculations of Self-Energies and Dielectric Response Functions of Solids. *Phys. Rev. Lett.* **1995**, *74*, 1827−1830.
(46) Bruneval, F.; Gonze, X. Accurate GW Self-Energies in a Plane-Wave Basis Using Only a Few Empty States: Towards Large Systems. *Phys. Rev. B: Condens. Matter Mater. Phys.* **2008**, *78*, 085125.
(47) Sajjad, M.; Singh, N.; Schwingenschlögl, U. Strongly Bound Excitons in Monolayer PtS2 and PtSe2. *Appl. Phys. Lett.* **2018**, *112*, 043101.
(48) By directly checking the stability of different stacking patterns, we identified the AA structure to be the most stable.
(49) Villaos, R. A. B.; Crisostomo, C. P.; Huang, Z.-Q.; Huang, S.-M.; Padama, A. A. B.; Albao, M. A.; Lin, H.; Chuang, F.-C. Thickness Dependent Electronic Properties of Pt Dichalcogenides. *npj 2D Mater. Appl.* **2019**, *3*, 2.
(50) Ahmad, S. Strain and Electric Field Dependent Variation in Electronic and Thermoelectric Properties of PtS2. *Results Phys.* **2020**, *17*, 103088.
(51) Carvalho, A.; Ribeiro, R. M.; Castro Neto, A. H. Band Nesting and the Optical Response of Two-Dimensional Semiconducting Transition Metal Dichalcogenides. *Phys. Rev. B: Condens. Matter Mater. Phys.* **2013**, *88*, 115205.
(52) Shi, H.; Yan, R.; Bertolazzi, S.; Brivio, J.; Gao, B.; Kis, A.; Jena, D.; Xing, H. G.; Huang, L. Exciton Dynamics in Suspended Monolayer and Few-Layer MoS22D Crystals. *ACS Nano* **2013**, *7*, 1072−1080.
(53) Sohier, T.; Campi, D.; Marzari, N.; Gibertini, M. Mobility of Two-Dimensional Materials From First Principles in an Accurate and Automated Framework. *Phys. Rev. Mater.* **2018**, *2*, 114010.
(54) Kuroda, T.; Hoshi, Y.; Masubuchi, S.; Okada, M.; Kitaura, R.; Watanabe, K.; Taniguchi, T.; Machida, T. Dark-state impact on the exciton recombination of WS2 monolayers as revealed by multi-timescale pump-probe spectroscopy. *Phys. Rev. B* **2020**, *102*, 195407.
(55) Jin, C.; Kim, J.; Utama, M. I. B.; Regan, E. C.; Kleemann, H.; Cai, H.; Shen, Y.; Shinner, M. J.; Sengupta, A.; Watanabe, K.; Taniguchi, T.; Tongay, S.; Zettl, A.; Wang, F. Imaging of pure spin-valley diffusion current in WS2-WSe2heterostructures. *Science* **2018**, *360*, 893−896.
(56) Mueller, T.; Malic, E. Exciton Physics and Device Application of Two-Dimensional Transition Metal Dichalcogenide Semiconductors. *npj 2D Mater. Appl.* **2018**, *2*, 29.
(57) Re Fiorentin, M.; Cicero, G.; Palummo, M. Spatially Indirect Excitons in Black and Blue Phosphorene Double Layers. *Phys. Rev. Mater.* **2020**, *4*, 074009.
(58) Jauregui, L. A.; Joe, A. Y.; Pistunova, K.; Wild, D. S.; High, A. A.; Zhou, Y.; Scuri, G.; De Greve, K.; Sushko, A.; Yu, C.-H.; Taniguchi, T.; Watanabe, K.; Needleman, D. J.; Lukin, M. D.; Park, H.; Kim, P. Electrical Control of Interlayer Exciton Dynamics in Atomically Thin Heterostructures. *Science* **2019**, *366*, 870−875.

https://doi.org/10.1021/acsami.1c11245
ACS Appl. Mater. Interfaces 2021, 13, 43615−43621